Experimental and Numerical Investigations of Effects of HFQ Conditions on Forming of AA6082 B-pillar components

Jiaqi Li[1], *Ruiqiang* Zhang[1], *Jianguo* Lin[1,2], and *Zhusheng* Shi[1*]

[1]Department of Mechanical Engineering, Imperial College London, London SW7 2AZ, UK
[2]Department of Industrial and Systems Engineering, The Hong Kong Polytechnic University, ZS972, Hong Kong SAR, China

Abstract. In this study, forming tests that replicate industrial forming conditions were conducted to explore the effects of HFQ conditions on the forming performance of AA6082 aluminium alloy sheets. In these tests, B-pillar components of a commercial vehicle were produced under different conditions, followed by ARGUS measurements to capture the formed geometry and strain distributions. A set of constitutive equations based on continuum damage mechanics (CDM) was implemented into FE models to simulate the forming processes, and the simulation results were compared with experimental data to validate the model and investigate the forming conditions. It was found that lower forming speed and higher temperature are beneficial to the quality of the formed parts, and the defects during forming were successfully predicted by the numerical simulations. Good agreements between the experimental and simulated results were found from the case study of the B-pillar forming tests, indicating that the CDM-based model can be successfully applied in practical forming processes for designing and optimising the process parameters.

Keywords: Hot stamping; Formability; Lightweighting; Aluminium alloy.

1 Introduction

Lightweight materials play a crucial role in the automotive industry, where stringent environmental regulations and safety requirements have led to increasing adoption of high-strength aluminium alloys [1]. However, the limited formability of Al alloys at room temperature presents significant challenges in sheet metal forming processes [2]. To overcome these limitations, the Hot Form Quench (HFQ®) process has gained increasing attention as a promising method for manufacturing complex-shaped aluminium parts with improved formability and reduced springback [3].

The viscoplasticity, formability and damage behaviours of high-strength Al alloys are strongly influenced by the temperature and strain rate [4]. A comprehensive understanding of these properties is essential for optimising the metal forming process. Key process-related factors, such as potential defects in HFQed parts and the forming force required, are directly influenced by the material's constitutive behaviour. Numerical simulation serves as a powerful tool for analysing these effects, but the accuracy of such simulations heavily relies on the implementation of well-calibrated material models [5]. Over the years, various models have been developed to characterise the thermomechanical properties of Al alloys under hot deformation conditions [6, 7]. Recently, biaxial formability tests have been introduced to improve the accuracy of formability assessment under elevated temperature conditions [8]. These experimental results can be directly integrated to a unified viscoplastic model based on continuum damage mechanics (CDM) [9]. While this approach has been successfully applied to ultra-high-strength steels such as 22MnB5 [9], its application to high-strength Al alloys remains limited. Moreover, its effectiveness for industrial forming processes requires further validation.

This study investigates the effects of HFQ conditions, particularly forming speed and temperature, on the quality of the formed part through combination of experimental investigation and advanced numerical simulations. Forming tests replicating industrial processes were conducted on AA6082 aluminium alloy sheets and optical measurements were employed to capture the formed geometry and strain distributions. A set of CDM-based constitutive equations were implemented into finite element (FE) models to simulate the material behaviour during forming. The simulation results were compared with experimental data to evaluate the accuracy of the model.

2 Methods and procedures

2.1 B-pillar forming tests

The forming experimental setup comprised an ESH 25T press machine equipped with controlling system, a specially designed tool for manufacturing a B-pillar component, and a furnace for heating the sheet metal. The forming tool, mainly consisted of a die, a punch and

* Corresponding author: zhusheng.shi@imperial.ac.uk

© The Authors, published by EDP Sciences. This is an open access article distributed under the terms of the Creative Commons Attribution License 4.0 (https://creativecommons.org/licenses/by/4.0/).

a blank holder, was installed in the press machine. The materials used in the experiment were AA6082-T6 sheets with a dimension of 310 mm × 200 mm × 2 mm.

The forming tests were carried out at various temperatures and forming speeds, as listed in Table 1. Temperature was measured with K-type thermocouples, which were fixed through pre-drilled holes on the side of the sheets. The forming speed was controlled by the press machine. Prior to testing, Omega 35 high-temperature lubricant (Sovereign Lubricants, UK) was applied to the die and the punch. During the tests, the sheet metal was heated in the furnace to the solution heat treatment temperature of 535 °C and soaked for 60s. The sheet was then transferred and positioned between the die and the blank holder, where it cooled. Once the sheet reached the desired forming temperature, it was promptly deformed with a certain speed. The formed part was in-die quenched and then removed after it cooled down to room temperature. The overall thermal profile is illustrated in Fig. 1. The force and stroke data throughout deformation were automatically captured by the controlling software of the press machine, while temperature readings from the thermocouples were recorded using PicoLog software via a data logger.

Table 1. Conditions for B-pillar forming tests.

Forming speed (mm/s)	400 °C	440 °C	480 °C
50		√	
250	√	√	√
350		√	

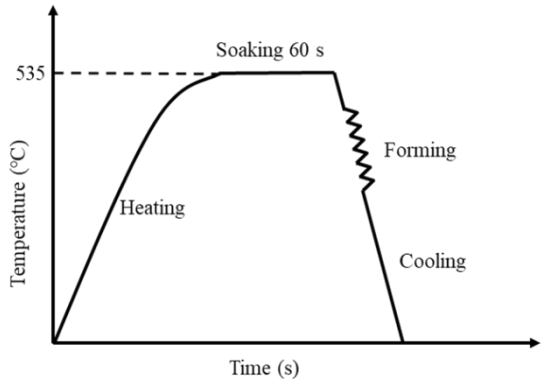

Fig. 1. Schematic thermal profile of the sheet metal during forming testing.

2.2 ARGUS strain measurement and analysis procedure for forming tests

The optical forming analysis system ARGUS was employed to measure the deformed shapes and the strain distributions of the formed parts. Before the test, metal sheets were marked with a dot pattern prepared by electro-chemical etching with an etching grid to produce reference features. In this test, the dots had a diameter of 0.75 mm and the grid spacing was 1.5 mm. After the forming tests, photographs of the formed parts were taken from various angles and heights. During the capturing process, the part was positioned on a turntable, surrounded by coded markers used for the spatial coordinate calibration (Fig. 2). The camera, mounted on a tripod, captured views from eight different angles and three heights by rotating the turntable and adjusting the height of the tripod.

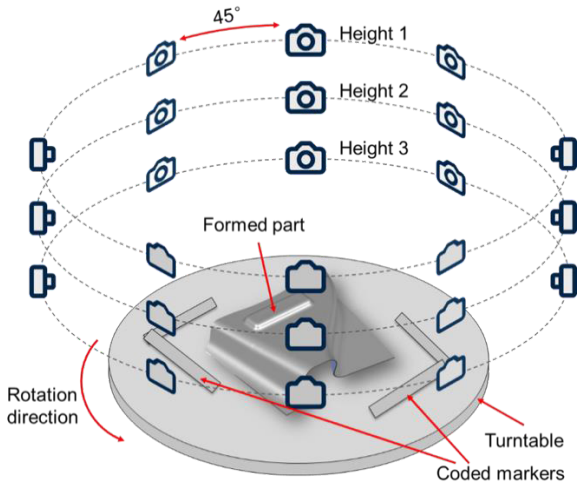

Fig. 2. Schematic of the ARGUS measurement. The formed part was put on a turntable with coded markers around it, and pictures were taken from different heights and different angles.

The photos were imported into the GOM ARGUS software for analysis. Based on predefined parameters of the lens and the coded markers, the software automatically identified the coded points and established the spatial coordinates according to their relative positions in different images, with supplementary manual matching. 3D surface geometries and strain distributions were subsequently computed by the software.

2.3 FE simulation

Finite element (FE) simulations were performed to investigate the effects of HFQ conditions on the formed parts. To simulate the damage degree in the forming process, the necking and fracture behaviours of the sheet metal should be defined in the constitutive equations and implemented in the FE program. To achieve this, a set of CDM-based constitutive equations proposed by Zhang et al. [9] was employed in this study. These equations are shown below:

$$\begin{cases} \dot{\varepsilon}_e^p = \left(\dfrac{\sigma_e - R - k}{K}\right)^{n_1} \dfrac{1}{(1-\omega_1)(1-\omega_2)^{\eta_1}} \\ \dot{R} = 0.5B\bar{\rho}^{-0.5}\dot{\bar{\rho}} \\ \dot{\bar{\rho}} = A(1-\bar{\rho})|\dot{\varepsilon}_e^p| - C\bar{\rho}^{n_2} \\ \dot{\varepsilon}_{ij}^p = \dfrac{3}{2}\dfrac{S_{ij}}{\sigma_e}\dot{\varepsilon}_e^p \\ \sigma_{ij} = D_{ijkl}\left(\varepsilon_{ij} - \varepsilon_{ij}^p\right) \\ \dot{\omega}_1 = \left[\dfrac{D_1}{(\mu_1 - 0.5\mu_2)^{\phi_1}}\right]\left(\dfrac{\mu_1\varepsilon_1 + \mu_2\varepsilon_2}{\gamma + \varepsilon_e^p}\right)^{\phi_1} \dfrac{1-\omega_1}{(1-\omega_2)^{\eta_1}}(\dot{\varepsilon}_e^p)^{\eta_2} \\ \dot{\omega}_2 = \left[\dfrac{D_2}{(\mu_1 - 0.5\mu_2)^{\phi_2}}\right]\left(\dfrac{\mu_1\varepsilon_1 + \mu_2\varepsilon_2}{\gamma + \varepsilon_e^p}\right)^{\phi_2} \dfrac{1}{(1-\omega_1)(1-\omega_2)^{\eta_1}}(\dot{\varepsilon}_e^p)^{\eta_2} \end{cases} \quad (1)$$

where σ_e is the effective stress, ε_e^p the effective plastic strain, ε_1 and ε_2 the major and minor in-plane strains, S_{ij} the components of the deviatoric stress tensor, R the stress due to isotropic hardening, k the initial yield stress, $\bar{\rho}$ the normalised dislocation density, D_{ijkl} the components of the elasticity tensor, and k, K, n_1, n_2, A,

B, C, D_1, D_2, μ_1, μ_2, ϕ_1, ϕ_2, η_1, η_2 and γ are material constants. The last two equations describe the evolution of two damage state variables ω_1 and ω_2. Critical values for ω_1 and ω_2 are set to 0.7, representing the threshold values for the onset of necking and fracture, respectively. The material constants k, K, n_1, B, D_1, μ_1, ϕ_1, η_2, D_2, ϕ_2 are temperature-dependent and take the form of

$$x = x_0 \exp\left(\frac{Q_x}{R_g T}\right) \quad (2)$$

where x represent the material constant, R_g the gas constant, which is equal to 8.314 J·K^{-1}·mol^{-1}, and Q_x is an energy term corresponding for x in the equation. C is also a temperature-dependent material constant and takes the form

$$C = C_0 \exp\left(\frac{-Q_c}{R_g T}\right) \quad (3)$$

Some of these material constants were determined by calibrating against the stress-strain curves obtained from uniaxial tests under different temperatures and strain rates. These calibrated constants are shown in Table 2.

Table 2. Calibrated material constants in the viscoplastic constitutive equations.

k_0 (MPa)	Q_k (J/mol)	K_0 (MPa)	Q_K (J/mol)	n_{1_0} (-)	Q_{n_1} (J/mol)
0.36	2.0×10^4	0.50	2.5×10^4	5.12	100.03
B_0 (MPa)	Q_B (J/mol)	A (-)	C_0 (s^{-1})	Q_C (J/mol)	n_2 (-)
1.00	1.9×10^4	0.10	5.00	2399	1.16

The damage-related parameters were determined by fitting the damage-related equations with the experimental data points for the limit strains obtained from biaxial formability tests. These constants are listed in Table 3.

Table 3. Calibrated damage-related constants.

D_{1_0} (-)	Q_{D_1} (J/mol)	μ_{1_0} (-)	Q_{μ_1} (J/mol)	μ_2 (-)
0.27	7388	0.31	210.8	0.15
ϕ_{1_0} (-)	Q_{ϕ_1} (J/mol)	γ (-)	η_1 (-)	η_{2_0} (-)
4.08	382.2	0.0035	5	0.99
Q_{η_2} (J/mol)	D_{2_0} (-)	Q_{D_2} (J/mol)	ϕ_{2_0} (-)	Q_{ϕ_2} (J/mol)
382.2	0.0225	5273	1.36	382.2

FE simulations were carried out using the commercial software Abaqus/Explicit to replicate the forming process under various forming temperatures and speeds. Fig. 3 shows the layout of the FE model used for the forming simulation. In this model, the punch, the die and the blank holder were treated as rigid bodies. Both the die and the blank holder were set completely fixed, meaning they had no displacement or rotation throughout the process, while the punch was allowed to move along the z-direction. When the simulation step started, the punch moved towards the sheet metal with a predefined forming speed, until the gap between the punch and the die matched the thickness of the sheet (2 mm). A friction coefficient of 0.3 was applied to the contact surfaces between the blank and the tools. The constitutive and damage models were implemented into the FE simulation using a VUMAT subroutine to describe the material behaviour and damage at various temperatures and strain rates.

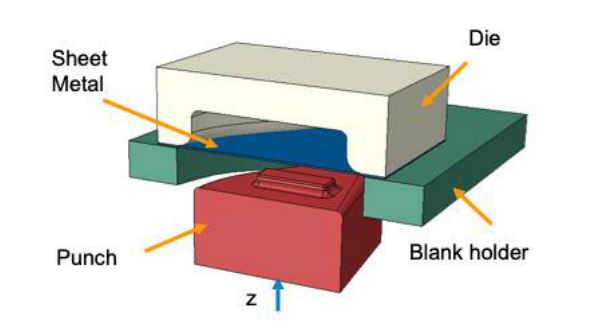

Fig. 3. Schematic FE model for forming the B-pillar part.

3 Results and discussion

3.1 Morphology of formed parts

While no macroscopic fracture was observed in the samples, necking was found occurred at the raised structure of the parts. To define the necking locations, two shorter edges at the upper part of the raised feature are labelled as Edge A and Edge B, with four vertices designated with a_1, a_2, b_1 and b_2, as shown in Fig. 4. It was observed that Edge A, located on the side nearer the curved shape, was more prone to necking, whereas no significant necking was found along Edge B on the opposite side.

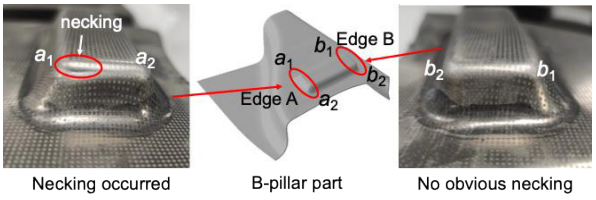

Fig. 4. The locations of necking occurred in the formed parts.

The results under various conditions are illustrated in Fig. 5, which reveal that the location and severity of necking are influenced by both temperature and forming speed. In some cases, such as the part manufactured at 400 °C and 440 °C under a forming speed of 250 mm/s, obvious necking can be spotted, while in other cases the necking appeared less significant or negligible. The necking locations under different conditions are summarised in Table 4. The data demonstrates a consistent trend: necking predominantly occurred along Edge A, particularly at Vertex a_1, which proved to be the most susceptible under conditions of lower temperatures and/or higher forming speeds. For example, in the part formed at 400 °C with a speed of 250 mm/s (Fig. 5(a)), necking not only concentrated at Vertex a_1 but extended toward Vertex a_2, indicating a more severe thinning along Edge A.

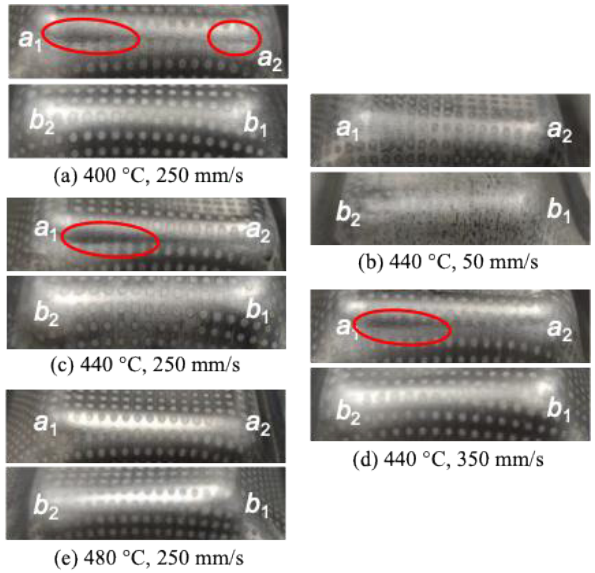

Fig. 5. The morphology of necking (labelled in circles) under different forming conditions.

Table 4. Necking locations.

Test #	Forming Temperature (°C) / Forming Speed (mm/s)	Necking location
1	400 / 250	a_1 a_2
2	400 / 250	a_1 a_2
3	440 / 50	a_1 (Slight)
4	440 / 50	None
5	440 / 250	a_1
6	440 / 250	a_1
7	440 / 350	a_1
8	440 / 350	a_1
9	480 / 250	a_1 (Slight)
10	480 / 250	a_1
11	480 / 250	a_1

In contrast, the vertices along Edge *B* (b_1 and b_2) consistently showed no significant necking across all forming conditions. Furthermore, forming at higher temperatures and lower speed, such as 440 °C at 50 mm/s or 480 °C at 250 mm/s, appeared to improve material ductility and alleviate stress concentrations, leading to higher part quality with minimal or negligible necking. This suggests that optimising the forming temperature and speed can effectively control necking and improve the uniformity of strain distribution in the final component.

The locations and extent of necking are attributed to the part's asymmetric geometry. Because the side with the curved shape has a longer and more complex profile, it requires greater material flow to achieve the desired contour. This increased material flow leads to higher stretching and strain concentration along Edge *A*, where the material is constrained by the surrounding features, amplifying the tendency for necking.

3.2 Forming force

In practical forming process, lower forming forces are typically preferred as they reduce tool wear, energy consumption, equipment requirement and overall production costs. Techniques such as hot stamping and HFQ are particularly beneficial in this regard, as they lower forming forces by operating within a temperature range where the sheet metal becomes soft and ductile, allowing for easier deformation and better formability. The blank holding force was recorded as -7.3 kN. Fig. 6 presents a typical history of force evolution and corresponding stroke. From the curve of recorded force, it is observed that the forming force suddenly increased when the die was closing and reached its maximum value when the die was closed, and then gradually decreased to a stable value during holding of the dieset due to the stress relaxation. Consequently, two characteristic forces, namely maximum force and holding force, were identified to evaluate the resistance of the sheet metal to deformation.

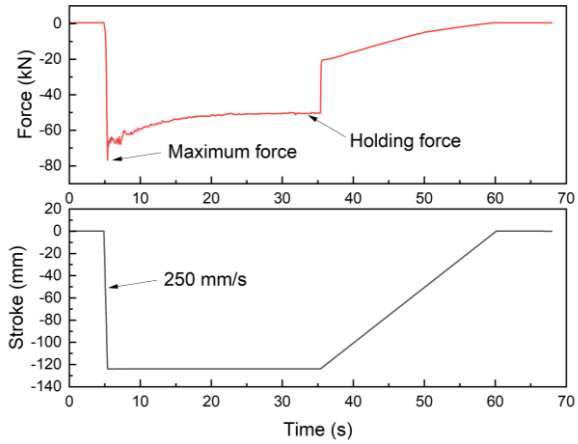

Fig. 6. Force and stroke during B-pillar forming, 440 °C, 250 mm/s.

Table 5 presents the average maximum forces and holding forces under various forming conditions. From the data, a clear trend emerges: higher temperatures and forming speeds generally result in lower forming forces, while lower temperatures and forming speeds lead to increased forces. For example, at 480 °C with a forming speed of 250 mm/s, the average maximum force was -70 kN, and the holding force was -37 kN. At a reduced temperature of 400°C, the maximum force increased significantly to -92.6 kN, with a holding force of -60.7 kN. The difference in forming forces at varied temperatures is likely due to reduced formability and increased resistance to deformation of the material at lower temperature. This trend also correlates with the observed occurrence of necking, as the material's formability is dependent on temperature. Lower forming temperatures and higher speeds make the material more prone to necking due to reduced ductility, while higher temperatures improve formability with more uniform material flow and reduce the risk of localised thinning.

Table 5. Forming forces.

Forming Temperature (°C) / Forming Speed (mm/s)	Maximum force (kN)	Force during holding (kN)
400 / 250	-92.6	-60.7
440 / 50	-90.0	-60.1
440 / 250	-75.1	-49.4
440 / 350	-75.8	-46.0
480 / 250	-70.0	-37.0

However, the relationship between forming speed and forming forces appears to contrast with the rate-effects on formability and necking behaviour. As indicated in Table 5, lower forming speeds result in higher maximum forming forces and holding forces, which seems counterintuitive given the reduced flow stress of sheet metal at lower strain rates. This discrepancy could possibly be attributed to frictional effects. This anomaly demonstrates the complex interplay of factors in the hot stamping process. It suggests that raising the forming temperature, rather than lowering the forming speed, can be a better strategy for improving formability, as the latter would bring side-effects of increased forming forces. By optimising both temperature and forming speed, it is possible to lower forming forces and minimise the likelihood of necking at the same time, contributing to improved quality in the formed components.

3.3 Strain distribution and FE simulation

B-pillar forming processes were simulated at different temperatures and forming speeds. Fig. 7 shows the simulated strain distributions of the formed part under different conditions, together with the experimental results. A good agreement was found between the simulated and experimental major strain distributions at different forming temperatures. In both experimental and simulated strain distributions, the location and the level of the maximum strain are almost the same, and the strain concentration was found at the corners of the raised feature, exhibiting a maximum major strain level of 0.8 to 1.0. In addition to the vertices, the four edges at the upper part of the raised feature also exhibited considerable strain concentration, with strain levels of approximately 0.4 to 0.6. It can also be noticed that the strain distributions were similar across different conditions, although slight difference were observed around the strain localisation spots.

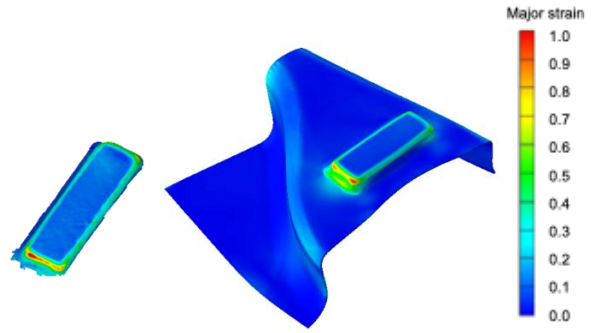

(a) 400 °C, 250 mm/s

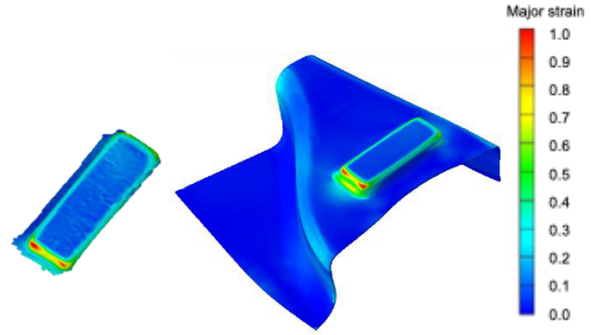

(b) 440 °C, 250 mm/s

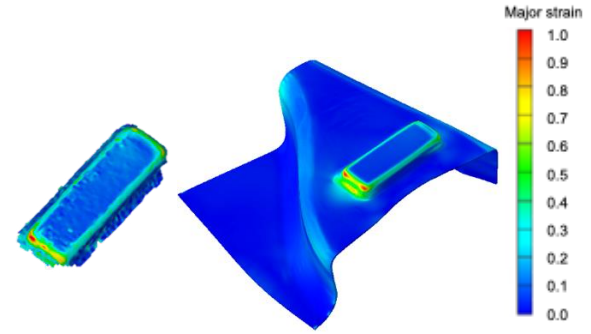

(c) 480 °C, 250 mm/s

Fig. 7. Experimental (left) and simulated (right) major strain distributions of the part formed under different conditions.

Fig. 8 illustrates the simulated results of necking locations in the formed parts after forming tests under different conditions. The necking areas are those where $\omega_1 \geq 0.7$ is reached, and are highlighted in red in the figure, while other areas ($\omega_1 < 0.7$) were coloured in blue. The results demonstrate that the trend of necking is in accordance with the experimental observations. As shown in Fig. 8 (a), (c), and (e), as the forming temperature increases, the extent of necking is less severe at higher forming temperatures and the necking area becomes significantly smaller. As the forming temperature increases from 400 °C to 480 °C, necking at vertices a_2, b_1 and b_2 gradually disappears. These trends perfectly align with the experimental findings presented in Table 2. Likewise, from Fig. 8 (b), (c), and (d), it is clear that a higher forming speed leads to more significant necking. The simulated necking locations closely match the experimental observations presented in Fig. 5, further validating the accuracy of the damage-related FE model in predicting necking behaviour under different forming conditions.

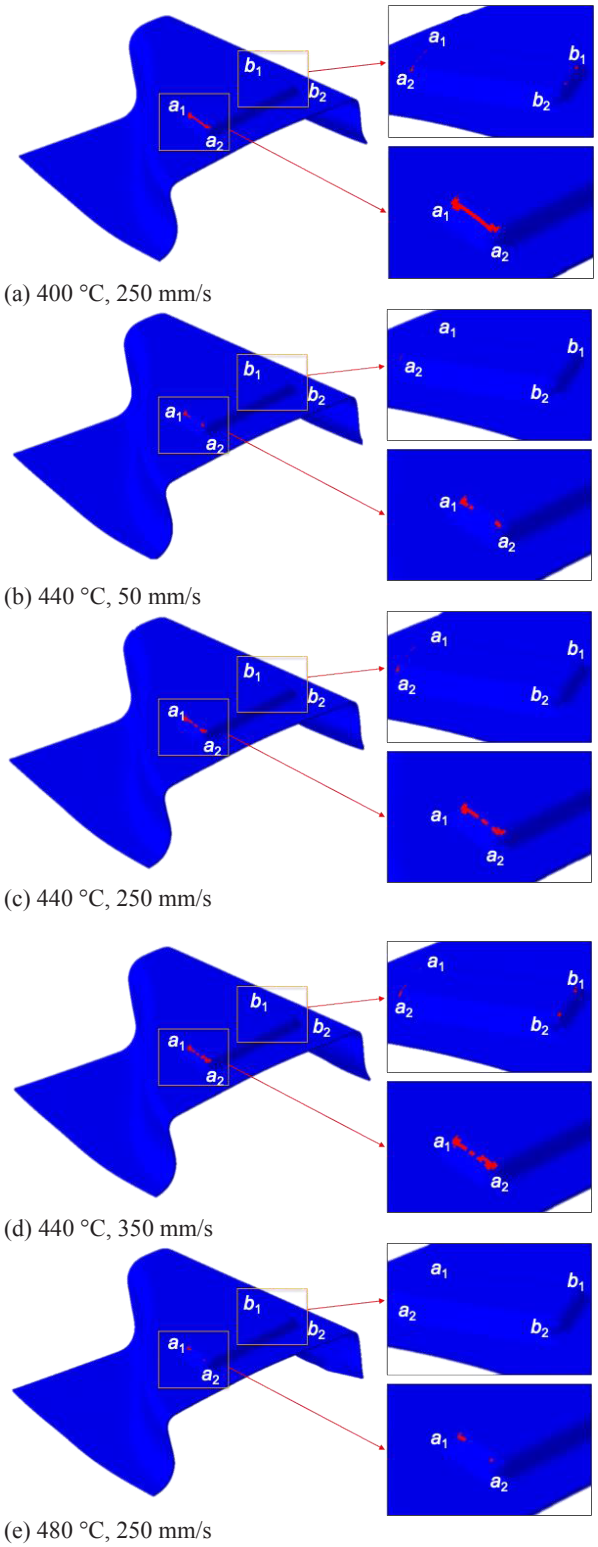

(a) 400 °C, 250 mm/s

(b) 440 °C, 50 mm/s

(c) 440 °C, 250 mm/s

(d) 440 °C, 350 mm/s

(e) 480 °C, 250 mm/s

Fig. 8. Locations of necking under different conditions.

4 Conclusions

Experimental investigation and FE simulations were carried out to study the HFQ processing of AA6082 B-pillar components. With a set of CDM-based constitutive equations, the FE simulations demonstrate their effectiveness in real-world forming processes. Experimental results showed that lower forming speeds and higher temperatures significantly improved part quality. Numerical simulations, incorporating CDM-based constitutive equations, accurately predicted strain distributions and defect locations, closely aligning with experimental data. This strong correlation validates the numerical model, confirming its reliability for predicting forming quality and optimising forming processes in industrial applications.

References

1. A. Taub, E. De Moor, A. Luo, D.K. Matlock, J.G. Speer, U. Vaidya, Annu. Rev. Mater. Res. **49**, 1 (2019)
2. K. Zheng, D.J. Politis, L. Wang, J. Lin, Int. J. Lightweight Mater. Manuf. **1,** 2 (2018)
3. A. Wang, K. Zhong, O. El Fakir, J. Liu, C. Sun, L.L. Wang, J. Lin, T.A. Dean, Int. J. Adv. Manuf. Technol. **89,** 5-8 (2017)
4. R. Gu, Q. Liu, S. Chen, W. Wang, X. Wei. J, Mater. Eng. Perform. **28,** 12 (2019)
5. M.A. Ablat, A. Qattawi, Int. J. Adv. Manuf. Technol. **89**, 1-4 (2017)
6. G. D'Amours, A. Ilinich, *Development of a material model for AA7075 aluminium hot stamping*, in 11th International Conference and Workshop on Numerical Simulation of 3D Sheet Metal Forming Processes, NUMISHEET, 30 Jul - 3 Aug 2018, Tokyo, Japan (2018)
7. Y. Guo, Y. Xie, D. Wang, L. Du, J. Zhao. J, Mater. Process. Technol. **296** (2021)
8. Z. Shao, N. Li, J. Lin, T.A. Dean, Exp. Mech. **56,** 9 (2016)
9. R. Zhang, Z. Shi, V.A. Yardley, J. Lin, Int. J. Damage Mech. **31,** 9 (2022)